

Advanced 3D Monte Carlo algorithms for bio-photonic and medical applications

Lewis McMillan



University of
St Andrews

This thesis is submitted in partial fulfilment for the degree of
PhD
at the
University of St Andrews

March 2019

Declaration

I, Lewis McMillan, hereby certify that this thesis, which is approximately ***** words in length, has been written by me, that it is the record of work carried out by me, or principally by myself in collaboration with others as acknowledged, and that it has not been submitted in any previous application for a higher degree.

I was admitted as a research student in September 2015 and as a candidate for the degree of PhD in September 2015; the higher study for which this is a record was carried out in the University of St Andrews between 2015 and 2019.

Date Signature of candidate

I hereby certify that the candidate has fulfilled the conditions of the Resolution and Regulations appropriate for the degree of PhD in the University of St Andrews and that the candidate is qualified to submit this thesis in application for that degree.

Date Signature of supervisor

Date Signature of supervisor

Abstract

Lorem ipsum dolor sit amet, consectetur adipiscing elit. Ut purus elit, vestibulum ut, placerat ac, adipiscing vitae, felis. Curabitur dictum gravida mauris. Nam arcu libero, nonummy eget, consectetur id, vulputate a, magna. Donec vehicula augue eu neque. Pellentesque habitant morbi tristique senectus et netus et malesuada fames ac turpis egestas. Mauris ut leo. Cras viverra metus rhoncus sem. Nulla et lectus vestibulum urna fringilla ultrices. Phasellus eu tellus sit amet tortor gravida placerat. Integer sapien est, iaculis in, pretium quis, viverra ac, nunc. Praesent eget sem vel leo ultrices bibendum. Aenean faucibus. Morbi dolor nulla, malesuada eu, pulvinar at, mollis ac, nulla. Curabitur auctor semper nulla. Donec varius orci eget risus. Duis nibh mi, congue eu, accumsan eleifend, sagittis quis, diam. Duis eget orci sit amet orci dignissim rutrum.

Nam dui ligula, fringilla a, euismod sodales, sollicitudin vel, wisi. Morbi auctor lorem non justo. Nam lacus libero, pretium at, lobortis vitae, ultricies et, tellus. Donec aliquet, tortor sed accumsan bibendum, erat ligula aliquet magna, vitae ornare odio metus a mi. Morbi ac orci et nisl hendrerit mollis. Suspendisse ut massa. Cras nec ante. Pellentesque a nulla. Cum sociis natoque penatibus et magnis dis parturient montes, nascetur ridiculus mus. Aliquam tincidunt urna. Nulla ullamcorper vestibulum turpis. Pellentesque cursus luctus mauris.

Contents

1 Monte Carlo radiation transport technique theory, code and validation	1
1.1 Introduction and Background	1
2 Computational modelling of tissue ablation	3
2.1 Introduction and background	3
2.2 Methods	4
2.2.1 Monte Carlo radiation transport (MCRT)	4
2.2.2 Heat transport	7
2.2.3 Tissue Damage	13
2.3 <i>In silca</i> results	15
2.3.1 Introduction	15
2.4 Conclusion	16

Chapter 1

Monte Carlo radiation transport technique theory, code and validation

1.1 Introduction and Background

The Monte Carlo radiation transport technique is a stochastic method used to model the transport of particles through scattering and absorbing mediums.

The Monte Carlo method has its roots in Buffon's needle experiment of *date here*. This involved dropping needles over lines spaced L apart and counting how many needles intersect the lines.

The Monte Carlo method is used in various different disciplines. Ranging from use in the financial sector to predict share*more info* to use in statistical analysis to use in modern computer generated images (see Fig. 1.1) *ref for all methods*

The technique that makes up the bulk of this thesis, is the Monte Carlo radiation transport technique. This method was created *correct word?* at the tail end of world war 2 at Los Alamos, for the purpose of calculating neutron diffusion though shielding material *ref*. It has since found amyriad of applications from light transport through dusty clouds, modelling the propagation of proton through tissue for radiotherapy to light transport through tissue.

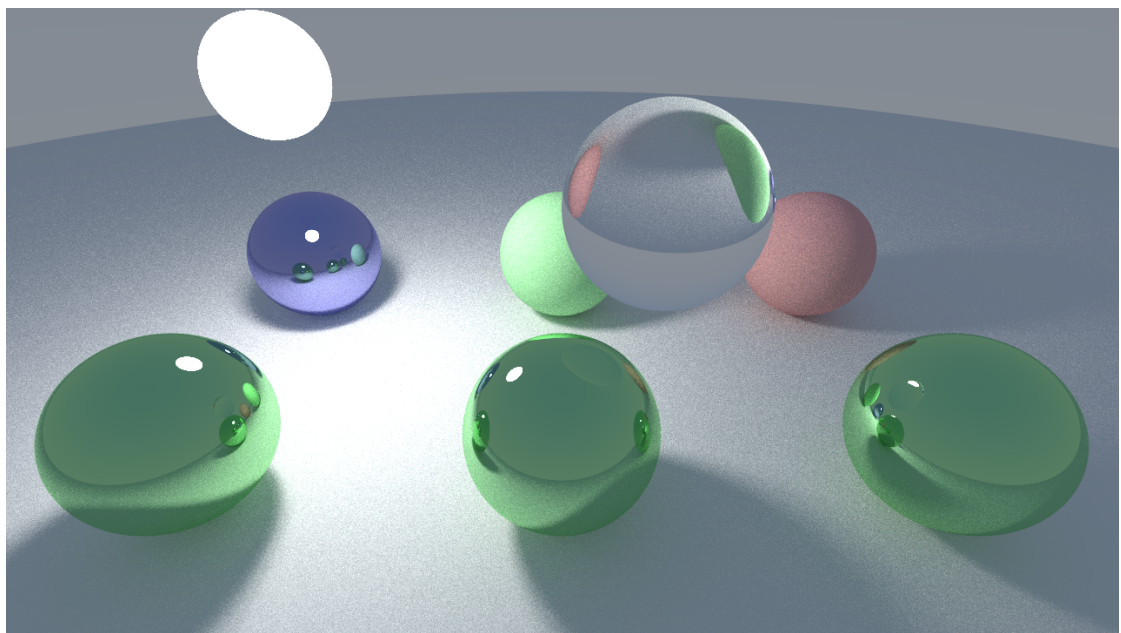


Figure 1.1: Computer generated imagery using ray-tracing. Code used to create image available at: github.com/lewisfish/RayTran

Chapter 2

Computational modelling of tissue ablation

2.1 Introduction and background

Lasers are used in wide variety of medical procedures not limited to: coagulating scalpels, port wine stain removal, tattoo removal, hair removal, and skin rejuvenation [1–5]. One class of laser used in these procedures are ablative lasers. Ablative lasers are usually high powered lasers targeted at a specific chromophore in the skin, to partially or fully remove layers of skin. These types of lasers are commonly used for aesthetic procedures such as: skin rejuvenation [5], and removal of various diseases such as Rhinophyma [6] or lesions/nodules [7]. They have also recently been investigated as a means of better drug delivery in the skin for photo-dynamic therapy (PDT) treatments [8].

One downside to using lasers to remove tissue, it that unlike a scalpel, where the surgeon has full control of the depth of the incision, ablative lasers are not as predictable. Lasers can also cause unwanted thermal damage to the surrounding areas, leading to unwanted effects. Ablative lasers, and fractionated ablative lasers (ablative lasers where the power is spread over several beams, such as to leave viable tissue around zones of damaged/necrotic tissue [9]). Currently the only reliable method to measure the depth of the ablative holes, is via a biopsy, which is an invasive procedure. We propose to use optical coherence tomography (OCT) to measure the ablative crater non-invasively *in-vivo*. The OCT measurements are then backed up by a computational model. This computational model could then be used to predict the depth of the ablative crater when using a certain power for various different applications such as: laser assisted drug delivery, and various cosmetic applications.

This chapter examines using Monte Carlo radiation transport techniques coupled to a heat transfer simulation, in order to study the thermal damage to tissue due to fractional lasers. We present experimental work carried out by our collaborators at the University of Dundee and the photobiology department at Ninewells hospital. This experimental work was carried out on porcine tissue, using CO₂ and Er:YAG lasers.

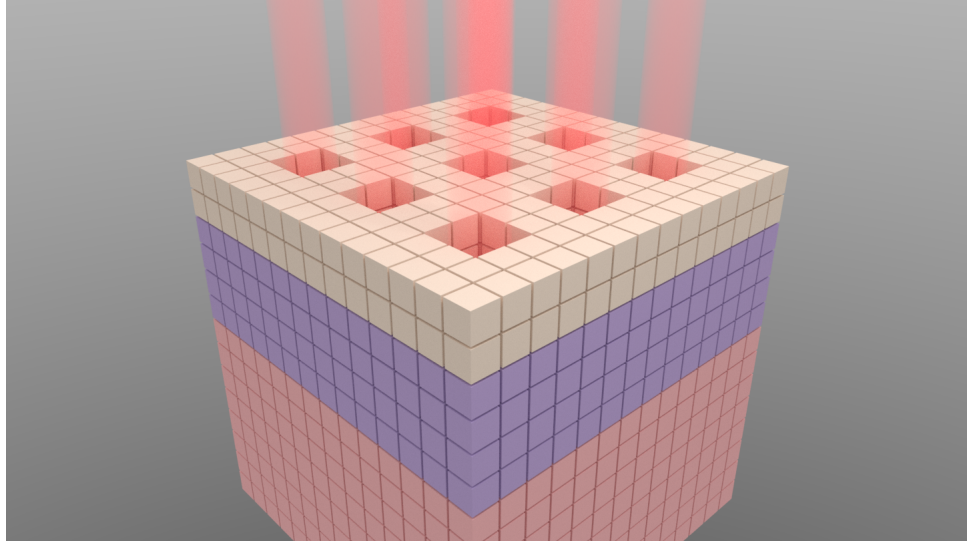


Figure 2.1: Example of a possible voxel model, with three different layers, various holes due to ablative pixel beam lasers. Each voxel represents a different optical/thermal property of the tissue medium.

2.2 Methods

In order to replicate the experimental work *in silica*, our numerical model has three main portions. The first is the Monte Carlo radiation transport method (MCRT) that models light transport through tissue so that we can calculate the laser energy deposited as a function of time and space. The second, a finite difference method (FDM) which is used to calculate the heat diffusion within the tissue due to the absorbed laser energy. Finally, a tissue damage model to track the damage to the tissue caused by the laser. All these individual portions are connected together to create our numerical model. Each portion of the numerical model is described below in more detail.

2.2.1 Monte Carlo radiation transport (MCRT)

MCRT is the ‘gold standard’ for simulating the transport of light through biological tissue *ref*. It uses interaction probabilities and random numbers in order to model the ‘random walk’ that photons undergo in a turbid medium. These ‘packets’ can undergo go scattering, absorption and various other physical process [10, 11]. MCRT has been used to model light-tissue interactions in many different medical and biophotonic applications [12]*more refs*. MCRT is used here to calculate the energy deposited by the laser, which is then passed to the heat transport simulation.

The tissue medium for the MCRT and heat transport simulations is a 3D voxel model (Fig. 2.1). This allows the variation of optical and thermal properties from voxel to voxel, making it the ideal type of grid for modelling tissue ablation. We use $n \times n \times n$ voxels *still changing this*, representing a tissue sample size of $1.1 \times 1.1 \times 0.5$ cm. We assume the porcine skin is uniform, so that initially our voxel model is uniform, and the optical properties of porcine skin at the wavelength of interest is that of water, see Fig. 2.9.

The original MCRT code was developed for astronomy applications [13, 14], and has since

been adapted for medical applications [12, 15].

Figure 2.2. shows the overall algorithm for the simulation, including the MCRT portion. The MCRT portion of the algorithm begins with determining where the photon enters the medium. This is calculated by randomly selecting one of the pixel beams, from the 9x9 array of pixel beams. Next the position on the surface of the medium is calculated. As the profile of the pixel beams are unknown, they are assumed to be uniformly circular *maybe change to gaussian??*. Thus, the packets position is uniformly sampled on a circle the width of the pixel beam.

Once the packet enters the simulation, a propagation distance for the packets is calculated using Eq. (2.1). The packet then moves this distance before undergoing an interaction event. This can be either scattering or absorption. This process is repeated until the photon has either been absorbed or exits the medium.

$$L = -\frac{\ln(\xi)}{\mu_a} \quad (2.1)$$

Where:

ξ a random number ($\tau = -\ln(\xi)$, τ is the optical depth);

μ_a is the absorption coefficient;

L is the physical distance.

Equation (2.1) is the equation for a uniform medium. As the medium we are simulating changes over time due to thermal damage this equation has to be adapted for a 3D Cartesian grid. Each voxel can have different optical properties, thus the photon packet is moved on a voxel by voxel basis. To start the movement process, a random number is generated, which is used to sample an optical depth the photon packet will travel. Next the photon enters the voxel and the maximum distance the photon can travel in the new voxel is calculated along the photons trajectory. If this optical distance is less than the optical depth sampled, then the photon enters the next voxel. If the distance is larger than the sampled optical distance then the photon has an interaction event in that voxel. The photon packet moves to the interaction event in the voxel and then undergoes scattering or absorption. The whole process is repeated until the photon ‘dies’ via absorption or leaving the medium.

This in turn is again repeated for all the photons, until all the photons have been absorbed or have escaped the tissue medium. We use 5 million photons per MCRT simulation run.

We calculate the absorbed energy using the path length counter method devised by Lucy [16]. The energy absorbed per voxel is calculated as:

$$E_i^{abs} = \frac{L}{N\Delta V_i} \sum \mu_a s \quad (2.2)$$

Where:

L is luminosity [W];

N is the number of photons;

ΔV_i is the volume of the i^{th} voxel [m^{-3}];

$\mu_{a,i}$ is the absorption coefficient of the i^{th} voxel [cm^{-1}];

and s is the pathlength of a photon packet through the i^{th} voxel [cm].

This grid of absorbed energy is then passed to the heat transport portion of the simulation.

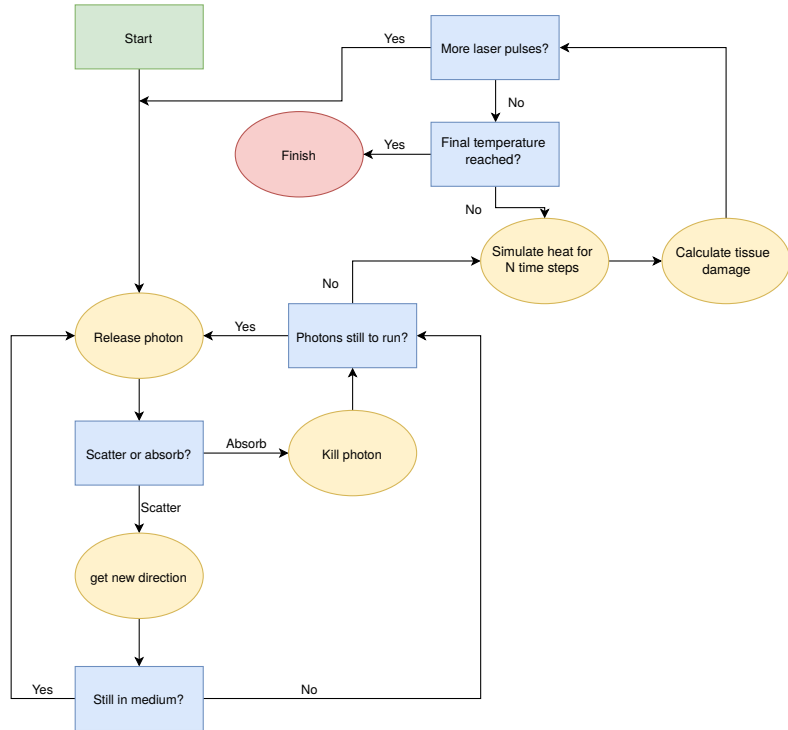


Figure 2.2: Flowchart of the tissue ablation algorithm.

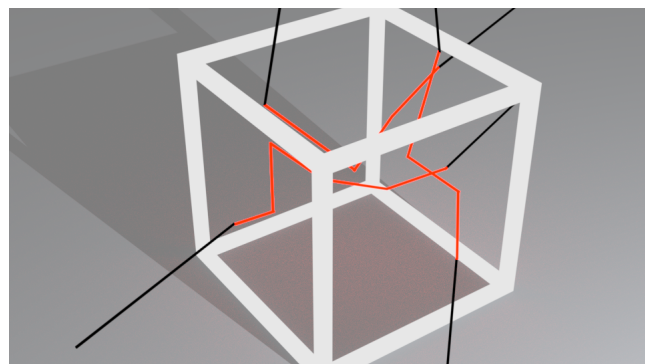


Figure 2.3: Red lines are photon paths within a voxel. Black lines photon paths outwith the voxel. Red photon paths are summed up in order to calculate the absorbed energy within each voxel.

2.2.2 Heat transport

In order to model the transport of heat in porcine skin, we use the standard parabolic heat equation:

$$\rho c_p \frac{\partial T}{\partial t} = \nabla \cdot (\kappa \nabla T) + \dot{q} \quad (2.3)$$

Where:

$T(x, y, z, t)$ is the temperature as a function of time and space [K];

κ is the thermal conductivity [$W \cdot m^{-1} \cdot K^{-1}$];

ρ is the density [$Kg \cdot m^{-3}$];

c_p the specific heat capacity [$J \cdot K^{-1}$];

$\dot{q}(x, y, z, t)$ is the source/sink term as a function of time and space [$W \cdot m^{-3}$].

As the medium changes as a function of temperature and time, we cannot make the assumption that κ , ρ , and c_p are constant and thus we have to solve the non-linear heat equation (Eq. (2.4)).

$$\frac{\partial T}{\partial t} = \frac{1}{(\rho c_p)_\xi} (\nabla k T + k \nabla^2 T) + \dot{q} \quad \xi = (i, j, k) \quad (2.4)$$

The \dot{q} term is a heat source/sink term. The heat source in this simulation is due to the laser, and we assume the only loss of heat to the surrounding medium is via convection and conduction.

These boundary conditions must be considered. All faces of the cube, bar the laser facing face, are considered to be pinned at $5^\circ C$, as the porcine skin was kept cooled prior to experimental work. The laser facing face has a simple convective BC:

$$\dot{q}_c = -hA(T - T_\infty) \quad (2.5)$$

Where:

h is the heat transfer coefficient [$Wm^{-2}K$];

and A is the area of the grid element, that is radiating/convicting heat away [m^{-2}].

As Eq. (2.4) is generally hard to solve in arbitrary geometries with complex boundary conditions we employ a numerical method to solve Eq. (2.4). The numerical method we employ in order to solve Eq. (2.3) is a the finite difference method (FDM) [17]. FDM is derived from the Taylor series approximation for derivatives. A function $f(x)$ is discretised onto a grid with N nodes (see Fig. 2.4). Then at node i we can use the Taylor series approximation in the forward (+ive x direction) and backward (-ive x direction), and combine the 1st and 2nd derivatives in 1D, where: i is the grid point at x_o , $i+1$ is the point at $x_0 + \Delta x$, and $i-1$ is the grid point at $x_o - \Delta x$.

$$\frac{df}{dx} = \frac{f_{i+1} - f_i}{\Delta x} \quad (forward) \quad (2.6a)$$

$$\frac{df}{dx} = \frac{f_i - f_{i-1}}{\Delta x} \quad (backward) \quad (2.6b)$$

$$\frac{df}{dx} = \frac{f_{i+1} - f_{i-1}}{2\Delta x} \quad (central) \quad (2.6c)$$

$$\frac{d^2 f}{dx^2} = \frac{f_{i-1} - 2f_i + f_{i+1}}{\Delta x^2} \quad (central) \quad (2.6d)$$

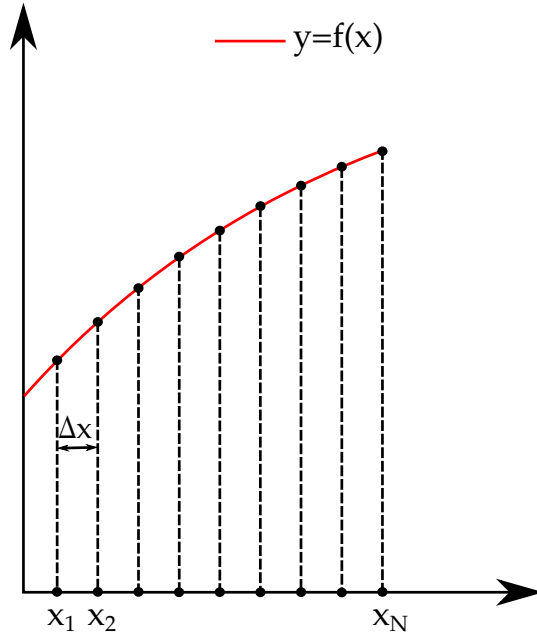


Figure 2.4: Finite difference methods discretisation of $f(x)$.

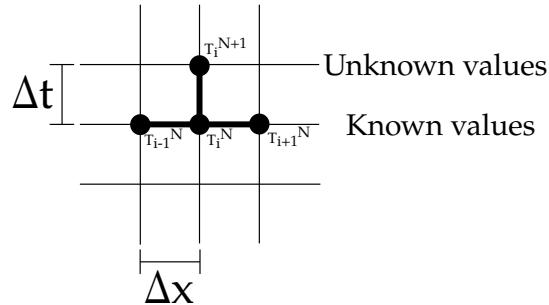


Figure 2.5: Finite difference method stencil for simple explicit scheme

Thus the linear heat equation Eq. (2.3), in 1D, becomes:

$$T_{i+1}^{n+1} = \Delta t \alpha \frac{T_{i-1}^n - 2T_i^n + T_{i+1}^n}{\Delta x^2} + T_i^n + \dot{q} \quad (2.7)$$

Equation (2.7) is called the ‘simple explicit form of finite-difference approximation’ [17]. Figure 2.5 shows the ‘stencil’ of this scheme, where there are three known points at time N , and just one unknown at time $N+1$. We use a simple explicit scheme here, due to its ease of implementation. For the more complicated non-linear heat equation we have to account for the change of the medium between points in the space and time. The simplest method of achieving this is to average κ, ρ , and c_p using a half difference scheme.

$$\kappa^\pm = \frac{\kappa_i + \kappa_{i\pm 1}}{2} \quad (2.8)$$

$$\rho^\pm = \frac{\rho_i + \rho_{i\pm 1}}{2} \quad (2.9)$$

$$c_p^\pm = \frac{c_{p,i} + c_{p,i\pm 1}}{2} \quad (2.10)$$

Yielding:

$$T^{N+1} = \Delta t(AT_{i-1}^N - 2BT_i^N + DT_{i+1}^N) + T_i^N + \dot{q} \quad (2.11)$$

Where:

$$\begin{aligned} A &= \frac{\kappa^-}{\rho^- c_p^- 2\Delta x^2} \\ B &= \frac{\kappa^+}{\rho^+ c_p^+ 2\Delta x^2} \\ D &= \frac{(A + B)}{2} \end{aligned} \quad (2.12)$$

For the more general 3D case, this yields:

$$U_{xx} = (AT_{i-1,j,k}^N - 2BT_{i,j,k}^N + DT_{i+1,j,k}^N) \quad (2.13)$$

$$U_{yy} = (AT_{i,j-1,k}^N - 2BT_{i,j,k}^N + DT_{i,j+1,k}^N) \quad (2.14)$$

$$U_{zz} = (AT_{i,j,k-1}^N - 2BT_{i,j,k}^N + DT_{i,j,k+1}^N) \quad (2.15)$$

$$T_{i,j,k}^{N+1} = \Delta t (U_{xx} + U_{yy} + U_{zz}) + T_{i,j,k}^N + \frac{\alpha \Delta t}{\kappa} q_L \quad (2.16)$$

Where:

$T_{i,j,k}^{N+1}$ is the new temperature at node i, j, k [K];

$T_{i,j,k}^N$ is the temperature at node i, j, k at the current time step [K];

α is the thermal diffusivity [$m^2 \cdot s^{-1}$];

κ is the thermal conductivity [$W/m \cdot K$];

Δx etc. is the size of the grid element in the p^{th} direction [m];

and A, B, D are the coefficients in their respective dimension (Eq. (2.12).)

Incorporating B.Cs on the top air exposed face:

$$U_{zz} = \frac{\alpha}{\Delta z^2} \left(\frac{2\Delta z}{\kappa} (-h(T_{i,j,k}^N - T_\infty^N)) - 2T_{i,j,k}^N + 2T_{i,j,k+1}^N \right) \quad (2.17)$$

As the lasers *maybe remove s?* operate in a pulsed mode, we account for this in our simulation. We assume that the pulse shape is a top-hat pulse for simplicity. In the heat simulation we have an additional variable in the term $laserOn \cdot \frac{\alpha \Delta t}{\kappa} q_L$ in Eq. (2.16). This additional variable, $laserOn$, is a boolean value, which is defined as:

$$laserOn = \begin{cases} 1, & \text{if time} \leq \text{pulse length} \\ 0, & \text{if time} > \text{pulse length.} \end{cases}$$

In the instance where there is more than one pulse, the laser is turned on and off based upon the pulse frequency.

As we are using a simple explicit FDM, the time step is constrained in order to make the solution stable. For a cubic 3D FDM without prescribed flux BCs, yields the constraint: $\Delta t \leq \frac{\alpha\Delta x^2}{2\beta}$. However as we have a flux prescribed boundary condition, the constraint on the time is more severe. Along with this time restraint, the pulse length of the laser also has to be considered. If the time step of the heat simulation is too large it will not account for the heat deposited by the laser. Thus, the timestep has to be an order of magnitude smaller than the shortest laser pulse.

As the timestep is small, and the grid resolution large, the resultant simulation is slow. Thus the code has been fully parallelised to improve performance. Both the MCRT and heat simulation are independently parallelised. As discussed in ??, the MCRT simulation is fully parallelised, and the results are passed to the heat simulation.

Parallelisation of the heat simulation is more involved than the ‘embarrassingly parallel’ class of problems that MCRT belongs to. This is due to the heat simulation needing to know the temperature of adjacent nodes. Thus information will have to be passed from each individual core during computation, as opposed to doing the information passing at the end of the simulation à la MCRT parallelisation.

The heat simulation is parallelised using a technique called ‘halo swapping’. This involves splitting up the computational domain (see Fig. 2.6), in this case the tissue medium, and doing the calculations on each domain on a separate core. The ‘halo swapping’ comes in when cores need to communicate with each other about updating their boundary temperature nodes (see Fig. 2.7).

On a workstation computer these simulations were carried out on (Intel Xeon E3-1245 v5, 8 core @3.5GHz) led to a speed up of ∼6, over the serial simulation. Using Amdahl’s law [18], the serial portion of the simulation is ∼ 5%, giving a theoretical speed up ∼ 20 times the serial simulation.

After the heat transport has been completed, the grid of temperatures is passed to the tissue damage portion of the simulation.

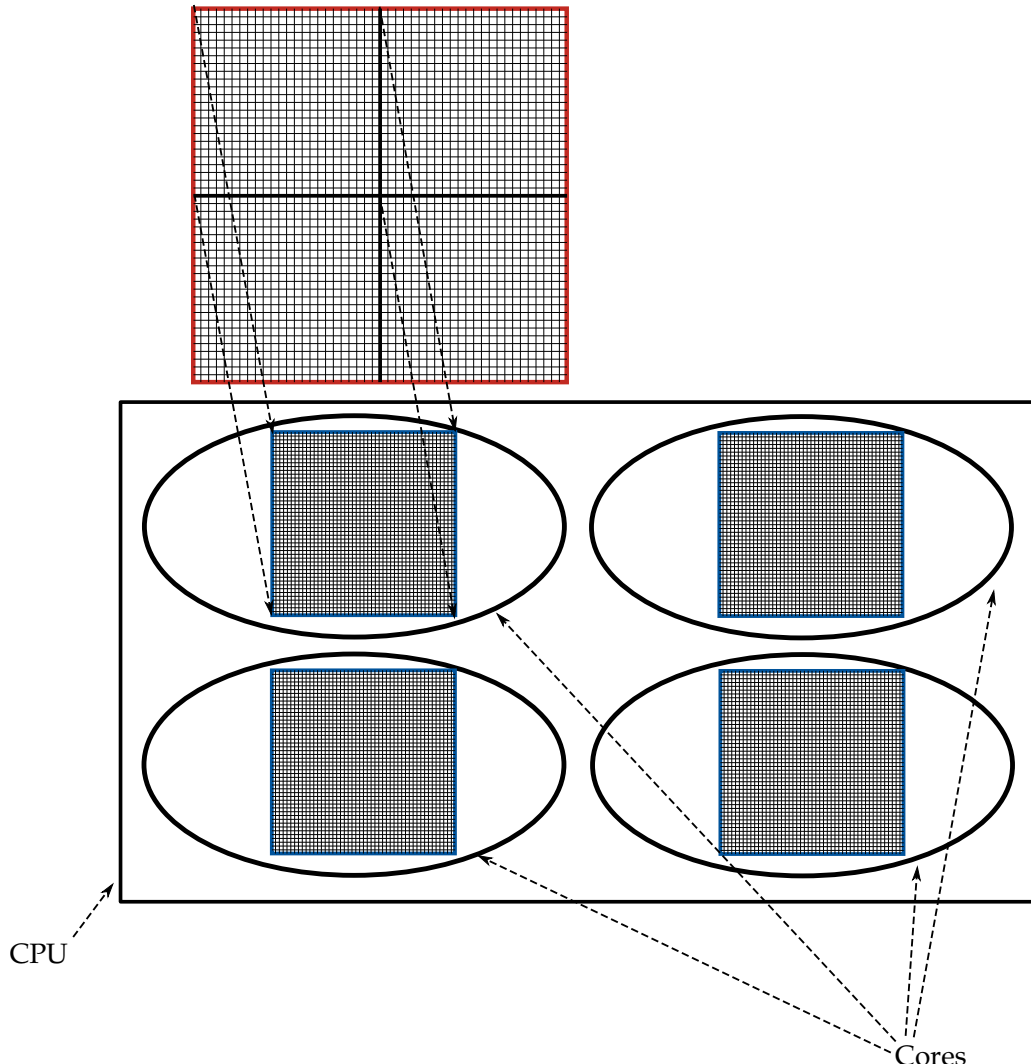


Figure 2.6: Computational domain decomposition. Total computational domain is evenly divided between cores in the CPU. This is done via layers of the domain in the z direction. Information is passed to/from cores via the ‘halo swap’ process (see Fig. 2.7).

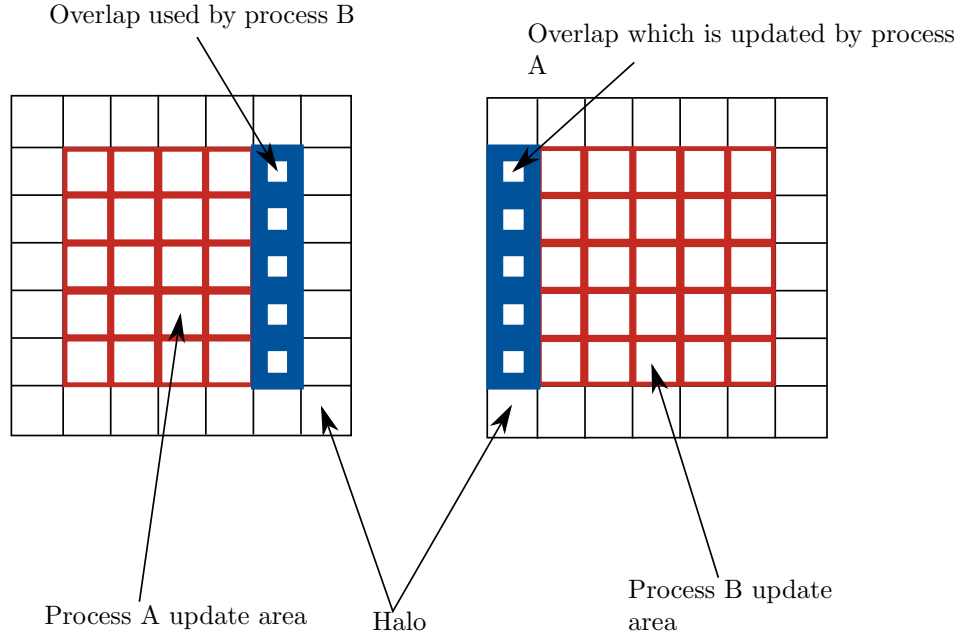


Figure 2.7: Halo swapping. Process A updates the area in red and blue on the left. It updates the blue area which is sent to process B as B's 'halo'. Process B cannot update its own halo, but rather updates the halo for process A.

Validation of heat transport numerical method

In order to validate the numerical method we employ to solve the heat equation, we compare the numerical method against an easily solvable case. We solve the heat equation on a cube, side L, in a surrounding medium of 0°C. The cube is initially at temperature 37°C and we calculate the temperature at time $t = \text{*input here*}$ s. Thus the boundary conditions are:

$$T(0, y, z, t) = T(x, 0, z, t) = T(x, y, 0, t) = 0^\circ\text{C} \quad (2.18)$$

$$T(L, y, z, t) = T(x, L, z, t) = T(x, y, L, t) = 0^\circ\text{C} \quad (2.19)$$

$$(2.20)$$

The thermal diffusivity (α)=, which corresponds to that of water *ref*.

Assuming a separable solution in Cartesian coordinates for the heat equation yields:

$$\begin{aligned} T(x, y, z, t) = & (A_1 \cos(\alpha x) + A_1 \sin(\alpha x)) \cdot \\ & (B_1 \cos(\beta y) + B_1 \sin(\beta y)) \cdot \\ & (C_1 \cos(\gamma z) + C_1 \sin(\gamma z)) \cdot e^{-\alpha \mu^2 t} \end{aligned} \quad (2.21)$$

$$\mu^2 = \alpha^2 + \beta^2 + \gamma^2 \quad (2.22)$$

Applying the boundary conditions (Eqs. (2.18) and (2.19)) gives:

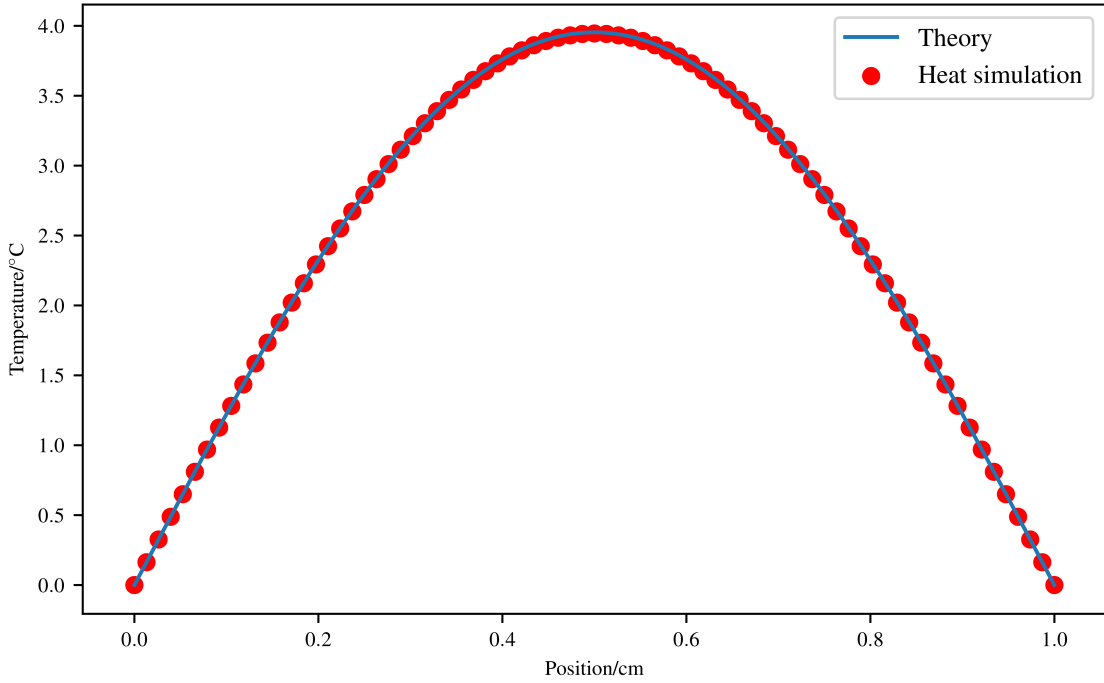


Figure 2.8: Comparison between analytical solution and numerical method.

$$A_1 = B_1 = C_1 = 0 \text{ and } \alpha = \frac{\pi n}{L} \beta = \frac{\pi m}{L} \gamma = \frac{\pi p}{L} \quad (2.23)$$

$$\therefore T_{nmp}(x, y, z, t) = A_{nmp} \sin\left(\frac{\pi n x}{L}\right) \cdot \sin\left(\frac{\pi m y}{L}\right) \cdot \sin\left(\frac{\pi p z}{L}\right) \quad (2.24)$$

This yields the following solution for the heat equation using the principle of superposition:

$$T(x, y, z, t) = \sum_{n=1,3,\dots}^{\infty} \sum_{m=1,3,\dots}^{\infty} \sum_{p=1,3,\dots}^{\infty} \frac{2368}{\pi^3 nmp} \sin\left(\frac{\pi n x}{L}\right) \sin\left(\frac{\pi m y}{L}\right) \sin\left(\frac{\pi p z}{L}\right) e^{(-\lambda^2 t)} \quad (2.25)$$

Where:

$$\lambda^2 = \alpha\pi^2\left(\frac{n^2}{L^2} + \frac{m^2}{L^2} + \frac{p^2}{L^2}\right);$$

n, m, p are odd integers;

and L is the length of the cube.

At time, $t = *input*s$, a slice through the middle of the cube, $L = 1 \text{ cm}$, yields Fig. 2.8.

2.2.3 Tissue Damage

The final portion of the simulation is the tissue damage model. We use the Arrhenius damage model, originally used as a kinetic model of reaction products in chemistry [19]. It has since been adapted by various authors for modelling tissue damage [20, 21].

$$\Omega(t) = \int_{t_i}^{t_f} A e^{-\frac{\Delta E}{RT}} d\tau \quad (2.26)$$

Where:

- Ω is the damage value;
- A is ‘frequency factor’ [s^{-1}];
- ΔE is activation energy [$J \cdot mol^{-1}$];
- R is the universal gas constant [$J \cdot mol^{-1} \cdot K^{-1}$];
- T is the temperature [K];
- and t_i and t_f are the initial time and final time at t_{crit} .

It is reported that a value of Ω of 0.53, 1.0, and 10^4 relate to first, second, and third degree burns respectively [22]. We use the Arrhenius damage model in order to better understand the amount of damage caused by the laser in the non-ablated areas of tissue. This can give us an insight into the various physical phenomena encountered in the OCT results.

We model tissue damage in three main sections: coagulated, dehydrated, and finally ablated sections.

Coagulated tissue is the the areas of the tissue where the temperature is above $43^\circ C$, the threshold for damage but below $100^\circ C$. When areas of the tissue reach $100^\circ C$ water begins to boil off. This acts as a large heat sink for the absorbed laser energy, slowing down the rate of ablation. The ener

$$Q_{vapor} = laserOn \cdot \dot{q} \cdot \Delta t \cdot V_{i,j,k} + c \cdot M_{i,j,k} \cdot \Delta T \quad (2.27)$$

Where:

- Q_{vapor} is the current energy in Joules that has been used to boil off the water in the voxel [J];
- $laserOn$ is a boolean variable that determine if the laser is on or off [−];
- \dot{q} is the energy absorbed by the voxel due to the laser [$W \cdot m^{-3}$];
- Δt is the timestep [s];
- $V_{i,j,k}$ is the volume of the i^{th} , j^{th} , k^{th} voxel [m^3];
- c is the heat capacity of the voxel [$J \cdot K^{-1}$];
- $M_{i,j,k}$ is the mass of the i^{th} , j^{th} , k^{th} voxel [Kg];
- and ΔT is the change in temperature the voxel would undergo, if the water was not boiling off.

As water boils off, the water content of each voxel changes. This affects the absorption coefficient, density, thermal conductivity, and heat capacity. Each of these vary linearly with water content per voxel [23]:

$$W = W_{init} - \left(W_{init} \cdot \left(\frac{Q_{current}}{Q_{vaporisation}} \right) \right) \quad (2.28)$$

$$\rho = 6.16 \cdot 10^{-5} W + 9.38 \cdot 10^{-4} \quad (2.29)$$

$$c = 2.5 \cdot 10^3 W + 1.7 \cdot 10^3 \quad (2.30)$$

$$\kappa = \rho \cdot 10^{-3} (0.454 W + 0.174) \quad (2.31)$$

Where:

- W is the water content (i.e $W = 0.7$ equates to 70% water content);
- W_{init} is the initial water content;
- $Q_{current}$ is the total energy absorbed by the i^{th} voxel since the temperature reached $100^\circ C$ [J];

	Thermal conductivity, κ	Density, ρ	Heat capacity, c
Tissue	$\rho \cdot 10^{-3}(0.454 W + 0.174)$	$6.16 \cdot 10^{-5} W + 9.38 \cdot 10^{-4}$	$2.5 \cdot 10^3 W + 1.7 \cdot 10^3$
Air	$ae^{-b(T-273.15)} + c$	$\frac{p_{atm}}{R_{spec}T}$	1006

Table 2.1: blah blah

κ is the Thermal conductivity [$W \cdot m^{-1} \cdot K^{-1}$];
and c is the heat capacity [$J \cdot Kg^{-1} \cdot K^{-1}$].

We define the ablation temperature (T_a) as occurring between 173 and 450°C [24]. At the T_a the tissue is removed and set the thermal and density properties to that of air.

The tissue structure is then fed back to the MCRT model and the whole process repeats until the average temperature of the model is under 43°C. This process is outlined in Fig. 2.2.

2.3 *In silca* results

2.3.1 Introduction

In order to match the experimental results, we must first create as accurate model of the experimental setup *in silca*. However due to computational constraints, such as memory and time available, we must make some approximations to the experiment. The porcine skin in reality was a large thin slice of the top most layers of the skin. However as the area of interest is where the ablation occurs, we model the porcine skin as a cuboid, dimensions: $1.1 \times 1.1 \times 0.5$ cm. The initial temperature of the porcine skin is assumed to be around 5°, as the tissue was kept on ice. As mentioned in the previous sections, there are several unknowns in the model: T_a , water content, temperature of air after ablation. Therefore we run several models so that the full parameter space of these unknowns can be explored. Results from these *in silca* experiments are presented in this section along with a comparison of the model to the experimental work carried out in collaboration with the University of Dundee and the photobiology department at Ninewells hospital.

Optical & thermal properties

Both of the lasers used in the experimental work are infrared lasers, this means that the optical properties of the tissue are dominated by water absorption (see Fig. 2.9). The lasers used in the experiment are the Lynton lumina 576 Er:YAG, and the Pixel CO₂. The Er:YAG laser has a wavelength 2940 nm which corresponds to an absorption coefficient of water: $\sim 11200 \text{ cm}^{-1}$. The CO₂ laser has a wavelength 10.6 μm which corresponds to an absorption coefficient of $\sim 850 \text{ cm}^{-1}$. As the absorption coefficient is large, we assume that scattering is negligible at these wavelength. Table 2.1 summarises the thermal properties for tissue and air used in the simulations.

Both lasers were used in ‘Pixel beam’ mode. This means that the laser beam is split into an array of smaller beams. The Er:YAG laser used a pattern of 5 x 5 lasers, with the corners missing, giving a total of 21 ‘Pixel beams’. The CO₂ laser used an array of 81 pixel beams with no missing ‘Pixels’. The power of these lasers was varied through the experiment. For the Er:YAG laser, it delivered multiple pulses of either 350 mJ or 700 mJ depending on which operating mode it was in (low or high), up to an energy of 3500 mJ. This energy is split evenly over all

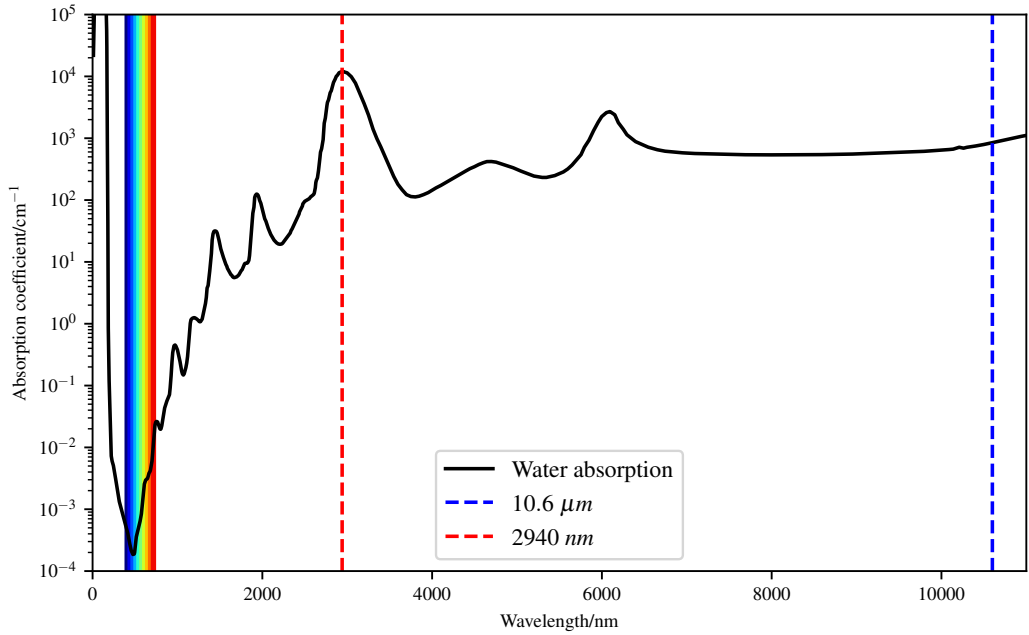


Figure 2.9: Water absorption coefficient for wavelengths 0-12000nm [25]. Data shows that water is highly absorbing at large wavelengths.

the pixel beams. The CO₂ laser used single pulses ('Super pulsed mode') of varying energy from 50 mJ to 400 mJ in increments of 25 mJ. This was for each individual 'Pixel beam'.

Investigating ablation temperature, T_a

Various literature sources report the ablation temperature ranging from 173° to 450°*cite this*. Thus, we run several models over this range. Fig. 2.10 shows how T_a affects the crater depth as a function of pixel beam energy. At lower pixel beam energies, the tissue ablation temperature has little to no effect on the crater depth. At higher energies, ≥ 125 mJ, the value of T_a has a larger effect. For example at 400 mJ there is a difference in the crater depth of ~ 0.05 mm between the lowest and highest T_a .

Investigating water content

Investigating temperature of air after ablation

2.4 Conclusion

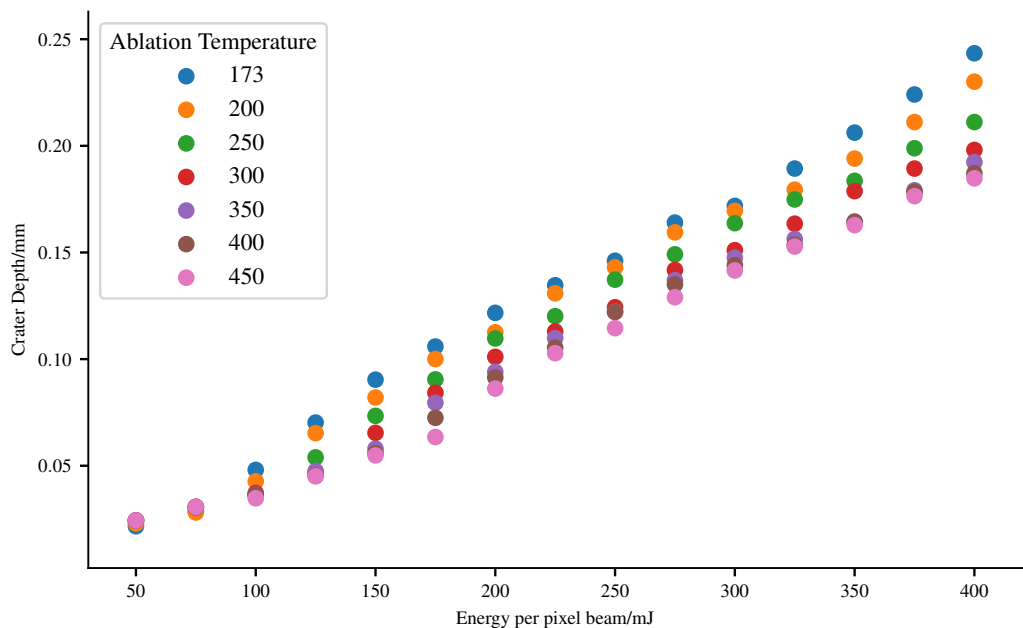


Figure 2.10: Simulation of CO_2 ablative laser crater depths as a function of pixel beam energy for various T_a s.

Bibliography

- [1] Saeid Amini-Nik, Darren Kraemer, Michael L Cowan, Keith Gunaratne, Puvindran Nadesan, Benjamin A Alman, and RJ Dwayne Miller. Ultrafast mid-ir laser scalpel: protein signals of the fundamental limits to minimally invasive surgery. *PLoS One*, 5(9):e13053, 2010.
- [2] Oon Tian Tan, Karen Sherwood, and Barbara A Gilchrest. Treatment of children with port-wine stains using the flashlamp-pulsed tunable dye laser. *New England journal of medicine*, 320(7):416–421, 1989.
- [3] Marina Kuperman-Beade, Vicki J Levine, and Robin Ashinoff. Laser removal of tattoos. *American journal of clinical dermatology*, 2(1):21–25, 2001.
- [4] Se Hwang Liew. Laser hair removal. *American journal of clinical dermatology*, 3(2):107–115, 2002.
- [5] Christina A Hardaway and E Victor Ross. Nonablative laser skin remodeling. *Dermatologic clinics*, 20(1):97–111, 2002.
- [6] Stanley M Shapshay, M Stuart Strong, Gaspar W Anastasi, and Charles W Vaughan. Removal of rhinophyma with the carbon dioxide laser: a preliminary report. *Archives of Otolaryngology*, 106(5):257–259, 1980.
- [7] Roberto Valcavi, Fabrizio Riganti, Angelo Bertani, Debora Formisano, and Claudio M Pacella. Percutaneous laser ablation of cold benign thyroid nodules: a 3-year follow-up study in 122 patients. *Thyroid*, 20(11):1253–1261, 2010.
- [8] Merete Haedersdal, Fernanda H Sakamoto, William A Farinelli, Apostolos G Doukas, Josh Tam, and R Rox Anderson. Fractional co₂ laser-assisted drug delivery. *Lasers in Surgery and Medicine: The Official Journal of the American Society for Laser Medicine and Surgery*, 42(2):113–122, 2010.
- [9] Dieter Manstein, G Scott Herron, R Kehl Sink, Heather Tanner, and R Rox Anderson. Fractional photothermolysis: a new concept for cutaneous remodeling using microscopic patterns of thermal injury. *Lasers in Surgery and Medicine: The Official Journal of the American Society for Laser Medicine and Surgery*, 34(5):426–438, 2004.
- [10] Gang Yao and Lihong V Wang. Monte carlo simulation of an optical coherence tomography signal in homogeneous turbid media. *Physics in Medicine & Biology*, 44(9):2307, 1999.
- [11] AJ Welch, Craig Gardner, Rebecca Richards-Kortum, Eric Chan, Glen Criswell, Josh Pfefer, and Steve Warren. Propagation of fluorescent light. *Lasers in Surgery and Medicine: The Official Journal of the American Society for Laser Medicine and Surgery*, 21(2):166–178, 1997.

- [12] Catherine Louise Campbell, Kenny Wood, RM Valentine, C Tom A Brown, and H Moseley. Monte carlo modelling of daylight activated photodynamic therapy. *Physics in Medicine & Biology*, 60(10):4059, 2015.
- [13] Kenneth Wood and RJ Reynolds. A model for the scattered light contribution and polarization of the diffuse $\text{H}\alpha$ galactic background. *The Astrophysical Journal*, 525(2):799, 1999.
- [14] Kenneth Wood, LM Haffner, RJ Reynolds, John S Mathis, and Greg Madsen. Estimating the porosity of the interstellar medium from three-dimensional photoionization modeling of HII regions. *The Astrophysical Journal*, 633(1):295, 2005.
- [15] Isla Rose Mary Barnard, Patrick Tierney, Catherine Louise Campbell, Lewis McMillan, Harry Moseley, Ewan Eadie, Christian Tom Alcuin Brown, and Kenneth Wood. Quantifying direct dna damage in the basal layer of skin exposed to uv radiation from sunbeds. *Photochemistry and photobiology*.
- [16] LB Lucy. Computing radiative equilibria with monte carlo techniques. *Astronomy and Astrophysics*, 344:282–288, 1999.
- [17] Necati Ozisik. *Finite difference methods in heat transfer*. CRC press, 1994.
- [18] Gene M Amdahl. Validity of the single processor approach to achieving large scale computing capabilities. In *Proceedings of the April 18-20, 1967, spring joint computer conference*, pages 483–485. ACM, 1967.
- [19] John A Pearce. Relationship between arrhenius models of thermal damage and the cem 43 thermal dose. In *Energy-based Treatment of Tissue and Assessment V*, volume 7181, page 718104. International Society for Optics and Photonics, 2009.
- [20] FC Jr Hendriques. Studies of thermal injury; the predictability and the significance of thermally induced rate processes leading to irreversible epidermal injury. *Arch. Pathol.(Chic)*, 43:489–502, 1947.
- [21] SC Jiang, N Ma, HJ Li, and XX Zhang. Effects of thermal properties and geometrical dimensions on skin burn injuries. *Burns*, 28(8):713–717, 2002.
- [22] KR Diller and LJ Hayes. A finite element model of burn injury in blood-perfused skin. *Journal of biomechanical engineering*, 105(3):300–307, 1983.
- [23] Bernard Choi and Ashley J Welch. Analysis of thermal relaxation during laser irradiation of tissue. *Lasers in Surgery and Medicine: The Official Journal of the American Society for Laser Medicine and Surgery*, 29(4):351–359, 2001.
- [24] Miron Gerstmann, Y Linenberg, Abraham Katzir, and Solange Akselrod. Char formation in tissue irradiated with a co 2 laser: model and simulations. *Optical Engineering*, 33(7):2343–2352, 1994.
- [25] David J Segelstein. *The complex refractive index of water*. PhD thesis, University of Missouri-Kansas City, 1981.